Coupled Functional Maps

Davide Eynard[†]   Emanuele Rodolà[†]   Klaus Glashoff[†]

Michael M. Bronstein[†‡⋆]

[†]USI Lugano   [‡]Tel Aviv University   [⋆]Intel

{davide.eynard, emanuele.rodola, klaus.glashoff, michael.bronstein}@usi.ch

Abstract

Classical formulations of the shape matching problem involve the definition of a matching cost that directly depends on the action of the desired map when applied to some input data. Such formulations are typically one-sided – they seek for a mapping from one shape to the other, but not vice versa. In this paper we consider an unbiased formulation of this problem, in which we solve simultaneously for a low-distortion map relating the two given shapes and its inverse. We phrase the problem in the spectral domain using the language of functional maps, resulting in an especially compact and efficient optimization problem. The benefits of our proposed regularization are especially evident in the scarce data *setting, where we demonstrate highly competitive results with respect to the state of the art.*

1. Introduction

Establishing correspondences between deformable shapes is a cornerstone problem in 3D computer vision and robotics, with applications ranging from texture mapping to object recognition and reconstruction. At its heart, the shape matching problem concerns the question of determining a map $\pi : \mathcal{X} \to \mathcal{Y}$ between two given shapes $\mathcal{X}$ and $\mathcal{Y}$, satisfying desirable properties for the task at hand. In computer graphics and 3D reconstruction, conformal (*i.e.*, angle preserving) maps are often required to preserve texture quality [16, 1]; for pose transfer and interpolation applications, one is interested in continuous maps [12] associating nearby points to nearby points; finally, for shape retrieval and registration, the interest shifts to maps having minimum metric distortion (near-isometries) [24].

A common denominator to this variety of approaches is the implicit and natural requirement for the existence of an *inverse* map $\pi^{-1} : \mathcal{Y} \to \mathcal{X}$, such that $(\pi \circ \pi^{-1})y = y$ for any point $y \in \mathcal{Y}$, and vice versa $(\pi^{-1} \circ \pi)x = x$ for any $x \in \mathcal{X}$. However, often due to algorithmic relaxations of the original matching problems, this property is rarely fulfilled by existing approaches – resulting in a substantial bias of the solutions in favor of one direction. An immediate consequence of this behavior is that the map quality will depend on the specific ordering of the shapes in input.

In this paper, we consider the shape matching problem in a new light: We propose a simple solution that considers the two mapping directions *simultaneously*, by putting equal weight on them. We demonstrate that this choice leads to maps of considerably higher quality than existing one-sided alternatives, while requiring significantly less data to drive the matching.

Related work. As mentioned previously, most shape matching approaches aim to minimize some notion of distortion among the input shapes, often depending on the application. Such distortion criteria include local feature similarity [27, 10, 2, 40, 21], geodesic [24, 7] or diffusion distances [11, 9, 30], or higher-order structures [41] (we refer to [36] for a recent survey). Windheuser *et al.* [38] proposed to model shapes as thin shells, and considered a symmetric formulation where they seek for a diffeomorphism with minimum physical deformation energy. Although their construction is unbiased, the resulting optimization problem is infeasible for shapes with more than 1K points. A recent trend is to use machine learning techniques to learn optimal point descriptors [39, 22, 5] and correspondences [33, 4], but these typically come with no theoretical guarantees on the final solutions.

Most related to our paper is the line of works based upon the notion of *soft correspondence*. Contrarily to traditional point-wise maps, soft maps assign to each point a continuous distribution (*e.g.*, a probability density) on the other shape, encoding a measure of "confidence" of the correspondence. Several approaches formulate the soft correspondence problem as one of mass transportation [23, 34] or Bayesian inference [37].

In this paper we build upon the *functional correspondence* framework, introduced by Ovsjanikov *et al.* [26] as a means to model the correspondence as a linear operator (named *functional map*) between functional spaces on the

two shapes. Such a choice leads to an especially compact representation of the map in the Laplacian eigenbases. In this representation, the problem of determining the correspondence is reduced to solving a linear system of equations, given some known set of corresponding functions (*e.g.*, descriptor fields) on the two shapes. This approach was extended in several follow-up works by imposing a prior on the geometric structure of the functional map matrix [29, 17], by simultaneous diagonalization of Laplacians [18], and by allowing partially similar shapes [31] among others. Huang *et al.* [14] considered functional map *networks* to encode structural similarities among multiple shapes in a collection. Their formulation seeks for cycle-consistent functional maps across the collection – namely maps that compose to the identity along any cycle. As we show in this paper, when applied to a pair of shapes their approach is equivalent to a relaxed version of our formulation.

Main contribution. In this paper we introduce a novel method for computing dense correspondences among deformable 3D shapes. Differently from most existing approaches, we simultaneously solve for the map going from one shape to the other, and the "coupled" map going in the inverse direction. Due to this property, we name our method *coupled functional maps*. Compared to the approaches of [26, 14], our algorithm provides better performances with a smaller computational effort. The advantage of our method is especially pronounced in the *scarce data* settings, when the problem becomes highly underdetermined. We further demonstrate how the joint optimization of the two maps has a "densifying" effect on the correspondence, giving rise to a better coverage of the two shapes.

The rest of the paper is organized as follows. Section 2 gives the necessary mathematical background on spectral geometry and functional maps. Section 3 presents our method, while Section 4 puts it in relation to existing approaches. Implementation details are given in Section 5. Experimental results are presented in Section 6, and finally, Section 7 concludes the paper.

2. Background

Notation. In this paper we use bold capital letters to denote matrices, bold lower-case letters for vectors, and italic lower-case letters for scalars. Given a matrix $\mathbf{A}$, we denote by $\|\mathbf{A}\|_{\mathrm{F}} = \left(\sum_{ij} a_{ij}^2 \right)^{1/2}$ its Frobenius norm, by $\|\mathbf{A}\|_{2,1} = \sum_j \left(\sum_i a_{ij}^2 \right)^{1/2}$ its $L_{2,1}$-norm, and by $\|\mathbf{A}\|_* = \sum_i \sigma_i$ its nuclear (or trace) norm, where $\sigma_1, \sigma_2, \ldots$ denote the singular values of $\mathbf{A}$.

Analysis on manifolds. We model shapes as compact connected 2-manifolds $\mathcal{X}$. Given $f, g : \mathcal{X} \to \mathbb{R}$ real scalar fields on the manifold, we define the standard inner product $\langle f, g \rangle_{L^2(\mathcal{X})} = \int_{\mathcal{X}} f(x)g(x)dx$, where integration is done using the area element induced by the Riemannian metric. We denote by $L^2(\mathcal{X}) = \{f : \mathcal{X} \to \mathbb{R} \mid \langle f, f \rangle_{L^2(\mathcal{X})} < \infty\}$ the space of square-integrable functions on $\mathcal{X}$.

The *intrinsic gradient* $\nabla_\mathcal{X} f$ and the positive semi-definite *Laplace-Beltrami operator* $\Delta_\mathcal{X} f = -\mathrm{div}_\mathcal{X}(\nabla_\mathcal{X} f)$ generalize the notions of gradient and Laplacian to manifolds. The Laplace-Beltrami operator admits an eigen-decomposition

$$\Delta_\mathcal{X} \phi_i(x) = \lambda_i \phi_i(x) \tag{1}$$

where $0 = \lambda_1 < \lambda_2 \leq \ldots$ are eigenvalues and $\phi_1, \phi_2, \ldots$ are the corresponding eigenfunctions. The eigenfunctions form an orthonormal basis on $L^2(\mathcal{X})$, *i.e.*, $\langle \phi_i, \phi_j \rangle_{L^2(\mathcal{X})} = \delta_{ij}$, generalizing the classical Fourier analysis: a function $f \in L^2(\mathcal{X})$ can be expanded into the *Fourier series* as

$$f(x) = \sum_{i \geq 1} \langle f, \phi_i \rangle_{L^2(\mathcal{X})} \phi_i(x). \tag{2}$$

Functional correspondence. Let us be now given two manifolds, $\mathcal{X}$ and $\mathcal{Y}$. Ovsjanikov *et al.* [26] proposed modeling *functional correspondence* between shapes as a linear operator $T : L^2(\mathcal{X}) \to L^2(\mathcal{Y})$. One can easily see that classical vertex-wise correspondence is a particular setting where T maps delta-functions to delta-functions.

Assuming to be given two orthonormal bases $\{\phi_i\}_{i \geq 1}$ and $\{\psi_i\}_{i \geq 1}$ on $L^2(\mathcal{X})$ and $L^2(\mathcal{Y})$ respectively, the functional correspondence can be expressed w.r.t. to these bases as follows:

$$
\begin{aligned}
Tf &= T \sum_{i \geq 1} \langle f, \phi_i \rangle_{L^2(\mathcal{X})} \phi_i = \sum_{i \geq 1} \langle f, \phi_i \rangle_{L^2(\mathcal{X})} T\phi_i \\
&= \sum_{ij \geq 1} \langle f, \phi_i \rangle_{L^2(\mathcal{X})} \underbrace{\langle T\phi_i, \psi_j \rangle_{L^2(\mathcal{Y})}}_{c_{ij}} \psi_j,
\end{aligned}
\tag{3}
$$

Thus, T amounts to a linear transformation of the Fourier coefficients of f from basis $\{\phi_i\}_{i \geq 1}$ to basis $\{\psi_i\}_{i \geq 1}$, which is captured by the coefficients c_{ij}. Truncating the Fourier series (3) at the first k coefficients, one obtains a rank-k approximation of T, represented in the bases $\{\phi_i, \psi_i\}_{i \geq 1}$ as a $k \times k$ matrix $\mathbf{C} = (c_{ij})$.

The spectral representation of the operator T as a matrix $\mathbf{C}$ allows manipulating correspondences in a convenient way as linear algebra operations. For example, given three manifolds $\mathcal{X}$, $\mathcal{Y}$ and $\mathcal{Z}$ and the correspondences $T_1 : L^2(\mathcal{X}) \to L^2(\mathcal{Y})$ and $T_2 : L^2(\mathcal{Y}) \to L^2(\mathcal{Z})$ expressed by the matrices $\mathbf{C}_1, \mathbf{C}_2$ in the respective bases, one can express the map $T_3 : L^2(\mathcal{X}) \to L^2(\mathcal{Z})$ as $\mathbf{C}_3 = \mathbf{C}_1 \mathbf{C}_2$.

In order to compute $\mathbf{C}$, Ovsjanikov *et al.* [26] assume to be given a set of q corresponding functions $\{f_1, \ldots, f_q\} \subseteq L^2(\mathcal{X})$ and $\{g_1, \ldots, g_q\} \subseteq L^2(\mathcal{Y})$. Denoting by $a_{ij} =$

$\langle f_i, \phi_j \rangle_{L^2(\mathcal{X})}$ and $b_{ij} = \langle g_i, \psi_j \rangle_{L^2(\mathcal{Y})}$ the $q \times k$ matrices of the respective Fourier coefficients, functional correspondence boils down to the linear system

$$\mathbf{AC} = \mathbf{B} . \qquad (4)$$

If $q \geq k$, the system (4) is (over-)determined and is solved in the least squares sense to find $\mathbf{C}$.

Structure of C. We note that the coefficients $\mathbf{C}$ depend on the choice of the bases. In particular, it is convenient to use the eigenfunctions of the Laplace-Beltrami operators of $\mathcal{X}$ and $\mathcal{Y}$ as the bases $\{\phi_i, \psi_i\}_{i \geq 1}$; truncating the series at the first k coefficients has the effect of 'low-pass' filtering thus producing smooth correspondences. In the following, this will be our tacit basis choice.

Furthermore, note that the system (4) has qk equations and k^2 variables. However, in many situations the actual number of variables is significantly smaller, as $\mathbf{C}$ manifests a certain structure that can be taken advantage of. In particular, if $\mathcal{X}$ and $\mathcal{Y}$ are isometric and have simple spectrum (*i.e.*, the Laplace-Beltrami eigenvalues have no multiplicity), then $T\phi_i = \pm\psi_i$, or in other words, $c_{ij} = \pm\delta_{ij}$. In more realistic scenarios (approximately isometric shapes), the matrix $\mathbf{C}$ would manifest a funnel-shaped structure, with the majority of elements distant from the diagonal close to zero.

With further assumption that the map T is area-preserving, Ovsjanikov *et al.* [26] show that the matrix $\mathbf{C}$ is orthogonal ($\mathbf{C}^\top \mathbf{C} = \mathbf{I}$). This fact was exploited by Kovnatsky *et al.* [18] to construct coupled bases via joint diagonalization of Laplacians.

Conversion to point-wise map. Functional maps represented by the matrix of spectral coefficients $\mathbf{C}$ can be converted to a point-wise map using any of the approaches described in [26, 32, 37]. For an unbiased analysis of the quality of the maps (and thus avoid the post-processing refinement of more sophisticated techniques) in this paper we follow the simple nearest-neighbor approach of Ovsjanikov et al. [26]. Specifically, let $\mathbf{\Phi}$ contain the eigenfunctions ϕ_i as its columns, and similarly for $\mathbf{\Psi}$. For each point $y \in \mathcal{Y}$ we consider its corresponding column in $\mathbf{\Psi}^\top$ (*i.e.*, the Fourier coefficients of a delta function δ_y supported at y), and look for the closest column in $\mathbf{C\Phi}^\top$ in the L_2 sense. The point $x \in \mathcal{X}$ associated to this column is marked as a match for y. By interpreting the matrices $\mathbf{\Phi}^\top, \mathbf{\Psi}^\top$ as the spectral embeddings of the two shapes in a k-dimensional Euclidean space, we see that the action of the functional map $\mathbf{C}$ is to align the two embeddings. The nearest-neighbor approach thus simply evaluates the point-wise proximity of the two spectral embeddings after application of the functional map. Note that this simple approach can generate one-to-many matches, as no bijectivity constraints are imposed during the recovery process.
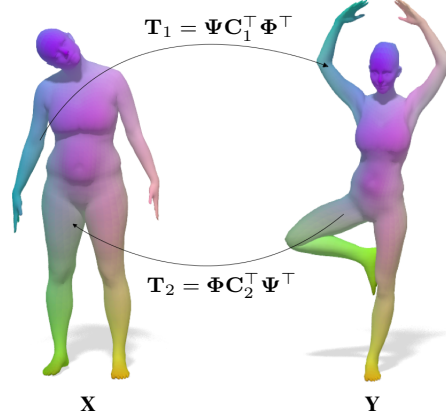

Figure 1. Our approach simultaneously solves for the two maps $\mathbf{T}_1, \mathbf{T}_2$, where $\mathbf{T}_2 \approx \mathbf{T}_1^{-1}$. Note that $\mathbf{T}_i$ and $\mathbf{C}_i$ encode the same functional map, with respect to different choices of a basis.

3. Coupled functional maps

The main idea of our paper is to simultaneously compute two maps, which we denote by $T_1 : L^2(\mathcal{X}) \to L^2(\mathcal{Y})$ and $T_2 : L^2(\mathcal{Y}) \to L^2(\mathcal{X})$, in a coupled manner. For some $f \in L^2(\mathcal{X})$ and $g \in L^2(\mathcal{Y})$,

$$T_1 f = \sum_{ij \geq 1} \langle f, \phi_i \rangle_{L^2(\mathcal{X})} \underbrace{\langle T_1 \phi_i, \psi_j \rangle_{L^2(\mathcal{Y})}}_{c^1_{ij}} \psi_j, \quad (5)$$

$$T_2 g = \sum_{ij \geq 1} \langle g, \psi_i \rangle_{L^2(\mathcal{Y})} \underbrace{\langle T_2 \psi_i, \phi_j \rangle_{L^2(\mathcal{X})}}_{c^2_{ij}} \phi_j \quad (6)$$

$$\begin{aligned} T_2 T_1 f &= \sum_{ijkl \geq 1} c^2_{ij} c^1_{kl} \phi_j \langle f, \phi_k \rangle_{L^2(\mathcal{X})} \langle \psi_i, \psi_l \rangle_{L^2(\mathcal{Y})} \\ &= \sum_{ijk \geq 1} c^1_{ki} c^2_{ij} \phi_j \langle f, \phi_k \rangle_{L^2(\mathcal{X})} \\ &= \sum_{k \geq 1} \phi_k \langle f, \phi_k \rangle_{L^2(\mathcal{X})} = f; \quad (7) \end{aligned}$$

it follows from the last coupling constraint that $\mathbf{C}_2 \mathbf{C}_1 = \mathbf{I}$. This leads us to the following system of equations

$$\begin{aligned} \mathbf{AC}_1 &= \mathbf{B} \\ \mathbf{A} &= \mathbf{BC}_2 \qquad (8) \\ \mathbf{C}_1 \mathbf{C}_2 &= \mathbf{I}. \end{aligned}$$

Note that this system is *non-linear* due to the coupling constraint.

We will show that approximately solving the system (8) instead of (4) improves the calculation of functional matrices noticeably, and analyze the reasons for it in the next section. In practice, to numerically solve problem (8), we minimize an expression of the form

$$\|\mathbf{AC}_1 - \mathbf{B}\| + \|\mathbf{A} - \mathbf{BC}_2\| \qquad (9)$$

FM	FMN	CFM	GT

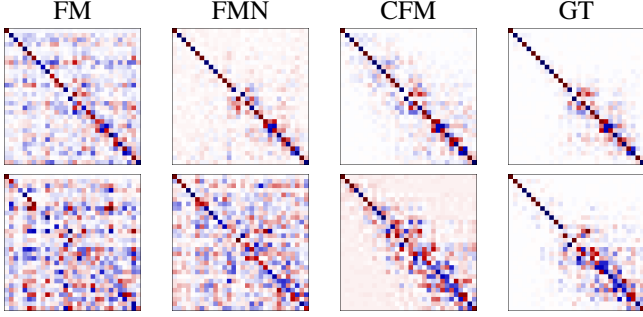Figure 2. **C** matrices obtained from two shape pairs (top: quasi-isometric, bottom: non-isometric) in the FAUST dataset by three different algorithms: functional maps (FM), functional map networks (FMN) and our method (CFM). Ground truth **C** is shown in the rightmost column as a reference.

subject to the constraints $\mathbf{C}_1\mathbf{C}_2 = \mathbf{I}$. Here there are different possibilities of choosing the norm in (9) and of the way one takes account of the constraints. In addition, regularization terms may make sense. In our formulation, we make use of the $L_{2,1}$- norm to be more robust to outliers, and we take account of the constraints by means of a penalty term:

$$\min_{\mathbf{C}_1,\mathbf{C}_2} \quad \|\mathbf{AC}_1 - \mathbf{B}\|_{2,1} + \|\mathbf{A} - \mathbf{BC}_2\|_{2,1} +$$
$$\mu_1\|\mathbf{C}_1\mathbf{C}_2 - \mathbf{I}\|_{\mathrm{F}}^2 + \mu_2 \sum_{i=1}^{2} \|\mathbf{C}_i \circ \mathbf{W}\|_{\mathrm{F}}^2 \quad (10)$$

where $\circ$ denotes Hadamard (element-wise) matrix product.

The μ_2-term models the structure of C with the weight matrix $\mathbf{W}$ (which is funnel shaped with zeroes along the diagonal and larger values outside, see Figure 2) and acts as a regularization, similar to the ones introduced in [29] and [31].
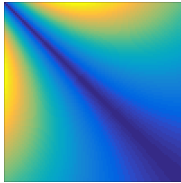
Finally, we note that the feasible set of our problem $\mathcal{M} = \{(\mathbf{X}, \mathbf{Y}) : \mathbf{X}^\top\mathbf{Y} = \mathbf{I}\}$ is a manifold (or more specifically, a sub-manifold of $\mathbb{R}^{n \times n} \times \mathbb{R}^{n \times n}$), and our problem can be approached by means of manifold optimization techniques [13]. We leave the development of such an approach to future research.

4. Relation to previous works

Relation to Ovsjanikov *et al*. [26] The baseline functional maps approach results in a linear system (4) of qk equations with k^2 variables. In order for the system to be determined, the size of the basis must be selected to satisfy $k \leq q$. In CFM, we consider two coupled systems (8) with $2k^2$ variables and $k(2q + k)$ equations. In order to obtain a determined system, we can have a basis twice as large, $k \leq 2q$. This effectively allows representing finer maps with a given amount of data.

Relation to Huang *et al*. [14]. Our approach can be seen as a special case of the method described in [14], on a functional map network of just two shapes and maps. There is, however, an important difference. The method of Huang *et al*. operates in two steps: (i) map computation via low-rank matrix recovery and (ii) latent basis function extraction. In the two-shapes setting, the authors solve (i) by constructing the matrix

$$\mathbf{Z} = \left(\begin{array}{cc} \mathbf{I} & \mathbf{C}_1 \\ \mathbf{C}_2 & \mathbf{I} \end{array} \right),$$

and computing the correspondences by solving the optimization problem

$$\min_{\mathbf{Z}} \|\mathbf{Z}\|_* + \|\mathbf{AC}_1 - \mathbf{B}\| + \|\mathbf{A} - \mathbf{BC}_2\|. \quad (11)$$

Due to non-smoothness of the nuclear norm, the authors resort to an ADMM technique involving singular value thresholding. Yet, problem (11) is a relaxed version of

$$\min_{\mathbf{Z}} \mathrm{rank}(\mathbf{Z}) \text{ s.t. } \left\{ \begin{array}{l} \mathbf{AC}_1 = \mathbf{B} \\ \mathbf{A} = \mathbf{BC}_2 \end{array} \right., \quad (12)$$

where the nuclear norm is used as a convex proxy for the rank, and the constraints are introduced as penalties with appropriate weights. By virtue of the following Lemma, we observe that Equation (12) is equivalent to our problem (8):

Lemma 1 *Let* $\mathbf{X}$ *and* $\mathbf{Y}$ *be* $n \times n$ *matrices. Then,* $\mathrm{rank}\left(\begin{array}{cc} \mathbf{I} & \mathbf{X} \\ \mathbf{Y} & \mathbf{I} \end{array} \right) = n$ *iff* $\mathbf{XY} = \mathbf{I}$.

Proof. We define the matrices

$$\mathbf{A} = \left(\begin{array}{cc} \mathbf{I} & \mathbf{0} \\ -\mathbf{Y} & \mathbf{I} \end{array} \right), \quad \mathbf{B} = \left(\begin{array}{cc} \mathbf{I} & -\mathbf{X} \\ \mathbf{0} & \mathbf{I} \end{array} \right),$$

which both have full rank $2n$ because of the identity matrices on their diagonals. Thus,

$$\mathrm{rank}(\mathbf{Z}) = \mathrm{rank}(\mathbf{AZB}) = \left(\begin{array}{cc} \mathbf{I} & \mathbf{0} \\ \mathbf{0} & \mathbf{I} - \mathbf{XY} \end{array} \right).$$

It follows that $\mathrm{rank}(\mathbf{Z}) \geq n$ and $\mathrm{rank}(\mathbf{Z}) = n$ iff $\mathbf{XY} = \mathbf{I}$.

We can thus conclude that Huang *et al*. solve, in the first step of their algorithm, a relaxed version of our problem, resorting to a computationally heavier approach. Moreover, we replace the second step with the μ_2-term shown in (10).

5. Implementation

We implemented our method in MATLAB[1] using the manifold optimization toolbox [6]. The optimization was performed using the nonlinear conjugate gradients method.

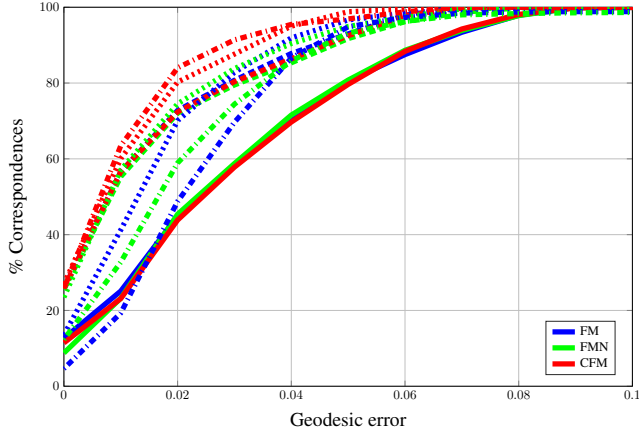[1]The code is available at http://vision.inf.usi.ch/EynRodGlaBro_3DV2016/

Figure 3. Correspondences on FAUST shapes measured using the Princeton protocol. Inputs are $q=50$ blobs, line styles match increasing values of $k = 40$ (solid), 80 (dashed), 120 (dotted), and 200 (dash-dot).

To speed up convergence, we initialized our method with the output of functional maps. In our experiments we observed convergence in less than 50 iterations ($<$1s for a pair of shapes).

We adopt the discretization of the Laplace-Beltrami operator [19] based on the classical cotangent weights [28, 25]:

$$s_{ij} = \begin{cases} -(\cot \alpha_{ij} + \cot \beta_{ij})/2 & ij \in E; \\ 0 & \text{otherwise,} \end{cases} \quad (13)$$

where α_{ij}, β_{ij} are the angles in front of the edge ij. The vertex weights are defined as local area elements $a_i = \frac{1}{3} \sum_{jk:ijk \in F} \text{area}(\mathbf{x}_i \mathbf{x}_j \mathbf{x}_k)$, equal to one third of the sum of the one-ring triangle areas.

This is followed by the computation of the first k non-constant eigenvectors ϕ_i of the generalized eigenvalue problem $\mathbf{S}\phi = \mathbf{D}\phi\Lambda$. Here $\mathbf{D}$ is the diagonal matrix of the vertex weights. The inner product is discretized as $\langle \mathbf{f}, \mathbf{g} \rangle = \mathbf{f}^\top \mathbf{D} \mathbf{g}$, where the vector $\mathbf{f} = (f(x_i))^\top$ represents a function on the surface (similarly for $\mathbf{g}$).

The $\mathbf{W}$ matrix we used for regularization was built following the formulation introduced in [31]:

$$w_{ij} = e^{-\sigma \sqrt{i^2 + j^2}} \| \frac{\mathbf{n}}{\|\mathbf{n}\|} \times ((i, j)^\top - \mathbf{p}) \|, \quad (14)$$

where $p = (1, 1)^\top$ is the matrix origin, $n = (1, 1)^\top$ is the direction of the diagonal, and $\sigma \in \mathbb{R}_+$ regulates the spread around the diagonal. In our experiments we set $\sigma = 0.03$ (see figure in Section 3).

The code of functional maps (FM) [26] and functional map networks (FMN) [14] we used in our experiments are, respectively, a CVX implementation of (4) and the original source code provided by the authors.
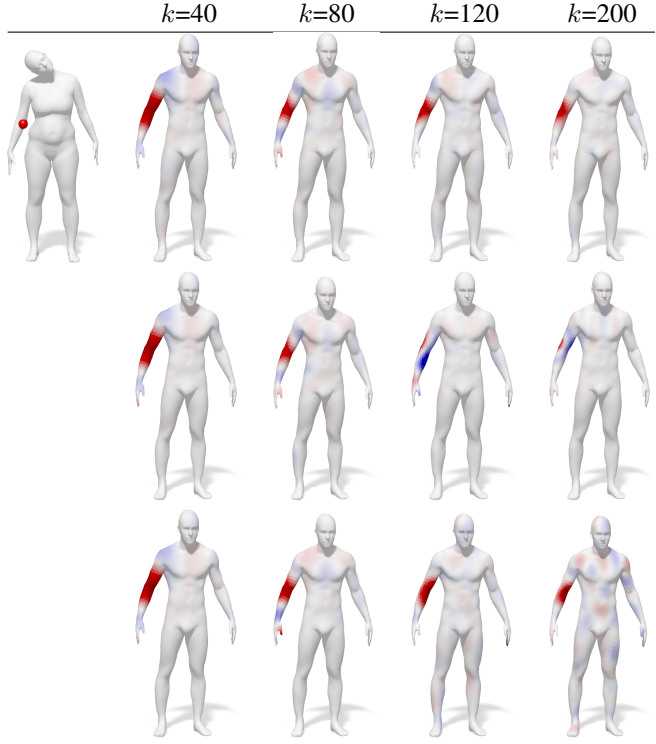

Figure 4. Mapping of a delta function from a FAUST shape to another, for different values of k (inputs are $q=50$ blobs). Top: FM, Middle: FMN, Bottom: CFM.

6. Results

Datasets. We used subsets of FAUST [3], containing scanned human shapes (6.9K vertices) in different poses, and TOSCA [8], containing higher-resolution synthetic shapes (27.8K vertices) of animals and humans. Both datasets provide vertex-wise correspondence between shapes (in TOSCA, only between shapes belonging to the same class).

Evaluation. To evaluate the correspondence quality, we used the Princeton protocol [15]. For a given tolerance r, we plot the percentage of correspondences falling within geodesic diameter r from the groundtruth correspondence.

Problem behavior. In our first experiment, we study the behavior of our problem following closely [17]. In particular, we are interested in the tradeoff between the basis size k and the dimensionality of the data (number of available correspondences) q. We used two human shapes from the FAUST dataset, providing as input data Gaussian blobs centered at $q=50$ corresponding vertices. Functional maps were computed using $k = 40$, 80, 120, and 200 Laplacian eigenvectors. We compared the performance of functional maps
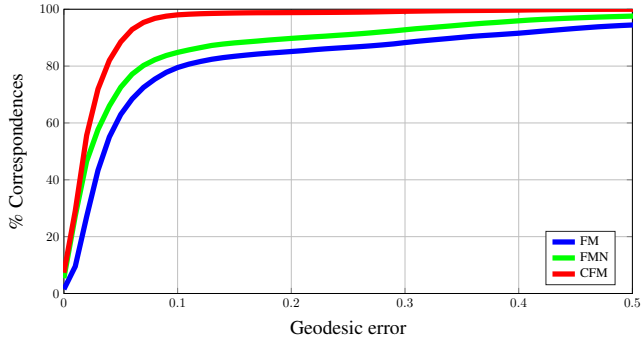
Figure 5. Correspondences on FAUST shapes using the Princeton protocol. Inputs are SHOT descriptors (q=320), k=30.

Figure 6. Correspondences on TOSCA shapes using the Princeton protocol. Inputs are SHOT descriptors (q=352), k=100.

(FM) [26], functional map networks (FMN) [14], and the proposed method (CFM).

The correspondence quality is visualized in Figure 3. In case $k = 40$, the problem is over-determined and all the methods produce nearly-equal results. Increasing k, the performance of FM and FMN first increases but then starts deteriorating. Conversely, the performance of CFM increases monotonously with the increase of k. This is evident in Figure 4, where a delta function on the reference shape is mapped to another shape using CFM with increasing values of k. Results show that with bigger k the mapped function is more localized and, at the same time, more precise than the one obtained with other approaches.

Shape correspondence. We performed the same experiment on the two datasets we took into consideration. For FAUST, we matched one shape (015) with 10 others, taken from different subjects in different poses (001, 012, 023, …, 090). For Tosca, we matched one shape (cat0) with 10 others from the same class in different poses. We used the extrinsic SHOT descriptors [35], computed using 9 normal bins (q=320) for FAUST and 10 for Tosca (q=352). We calculated face-based Laplacians as in [14] and the maps using the three methods FM, FMN, and CFM. The number of eigenfunctions we took into considerations were, respectively, k=30 for FAUST and k=100 for Tosca.

Figures 5 and 6 show the quality of our correspondences, measured quantitatively using the Princeton protocol. In both datasets we perform best, both obtaining a higher percentage of correct correspondences within a small geodesic diameter and saturating earlier than other methods. In terms of geodesic errors (see Figure 8), CFM has the best performance on isometric (leftmost column) and non-isometric shapes, keeping most of the errors below the threshold of 10% of the shape diameter. This is also reflected in Figure 9, where correspondence is shown by mapping a colormap from the reference shape to few others, and where our algorithm exhibits the smallest color distortion.
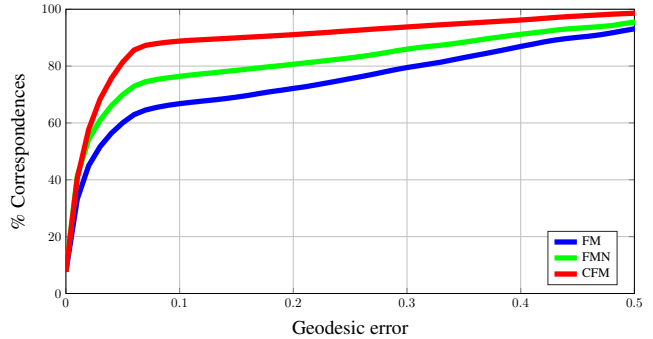

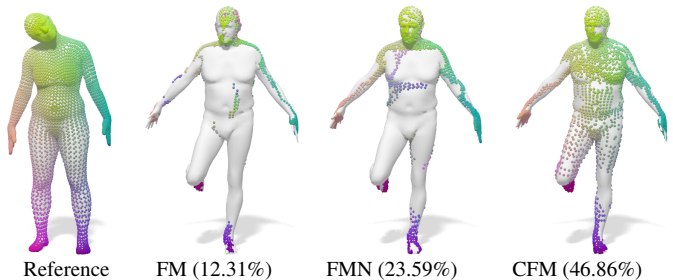| Reference | FM (12.31%) | FMN (23.59%) | CFM (46.86%) |

Figure 7. Displaying map surjectivity. The numbers in parentheses denote the percentage of surface area that is covered by the map, giving an indication as to how close the map is to a surjective one. Indirectly, this plot shows how well the map aligns the spectral embeddings of the two shapes.

Map surjectivity. In an ideal setting, one would like a map $\pi : \mathcal{X} \to \mathcal{Y}$ to be surjective, *i.e.*, such that every point $y \in \mathcal{Y}$ is the image of a point $x \in \mathcal{X}$ under π. This criterion can be used to show how well a given functional map aligns the spectral embeddings of two shapes: this is due to the fact that the nearest-neighbor approach used to convert a functional map into a point-wise map captures the quality of the alignment itself. In Figure 7 we show, for each method, how many points in the target shape have a corresponding one in the reference shape, and whether they are consistently located (color). CFM is, amongst the three evaluated maps, the one which is closest to surjectivity.

7. Conclusions

In this paper we introduced a novel algorithm for dense matching of deformable 3D shapes. Our method builds upon the intuition that solving *jointly* for the map and its inverse has a regularizing effect on the correspondence – resulting in maps that are more accurate, denser, and more efficient to compute than competing approaches on the same data. Importantly, our approach can be applied in situations where the amount of available data is very scarce.

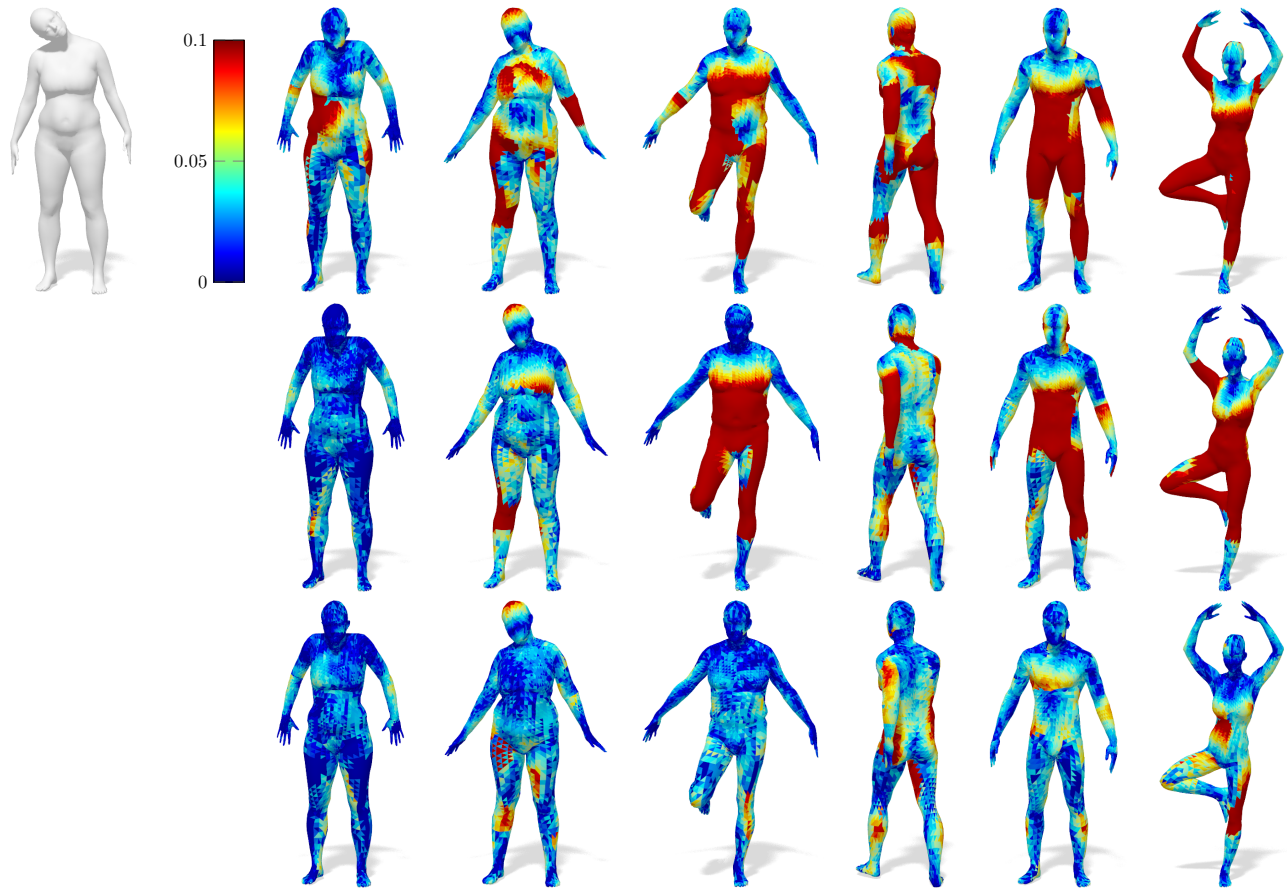**Future work.** Despite its simplicity, we believe that our

Figure 8. Correspondence quality on FAUST shapes shown as geodesic errors (from blue=small to red=large, saturated at 10% of the geodesic diameter). Top: FM, Middle: FMN, Bottom: CFM.

method can be adapted to a number of different scenarios as a powerful correspondence regularizer. A particularly promising application is partial functional correspondence [31, 20], where the shapes to be matched are allowed to have missing parts and the diagonal prior on **C** assumes a slanted structure. Second, in its current formulation our method makes use of large quadratic penalties in place of exact constraints. As noted in our discussion, the problem could be rephrased as an optimization on a biorthogonal manifold [13], leading to a more elegant and rigorous optimization than the one we proposed here. Exploring this possibility is an exciting direction of future research.

References

[1] N. Aigerman, R. Poranne, and Y. Lipman. Seamless surface mappings. *ACM Trans. Graphics*, 34(4):72:1–72:13, July 2015. 1

[2] M. Aubry, U. Schlickewei, and D. Cremers. The wave kernel signature: A quantum mechanical approach to shape analysis. In *Proc. 4DMOD*, 2011. 1

[3] F. Bogo, J. Romero, M. Loper, and M. J. Black. FAUST: Dataset and evaluation for 3D mesh registration. In *Proc. CVPR*, 2014. 5

[4] D. Boscaini, J. Masci, E. Rodolà, and M. M. Bronstein. Learning shape correspondence with anisotropic convolutional neural networks. In *Proc. NIPS*, 2016. 1

[5] D. Boscaini, J. Masci, E. Rodolà, M. M. Bronstein, and D. Cremers. Anisotropic diffusion descriptors. *Computer Graphics Forum*, 35(2), 2016. 1

[6] N. Boumal, B. Mishra, P.-A. Absil, and R. Sepulchre. Manopt, a Matlab toolbox for optimization on manifolds. *Journal of Machine Learning Research*, 15:1455–1459, 2014. 4

[7] A. M. Bronstein, M. M. Bronstein, and R. Kimmel. Generalized multidimensional scaling: a framework for isometry-invariant partial surface matching. *PNAS*, 103(5):1168–1172, 2006. 1

[8] A. M. Bronstein, M. M. Bronstein, and R. Kimmel. *Numerical Geometry of Non-Rigid Shapes*. Springer, 2008. 5

Figure 9. Qualitative example of correspondence (similar colors encode corresponding points, where the shape on top left is the reference) on the FAUST dataset. Compared methods are FM (top), FMN (middle), and CFM (bottom).

[9] A. M. Bronstein, M. M. Bronstein, R. Kimmel, M. Mahmoudi, and G. Sapiro. A Gromov-Hausdorff framework with diffusion geometry for topologically-robust non-rigid shape matching. *IJCV*, 89(2-3):266–286, 2010. 1

[10] M. M. Bronstein and I. Kokkinos. Scale-invariant heat kernel signatures for non-rigid shape recognition. In *Proc. CVPR*, 2010. 1

[11] R. R. Coifman, S. Lafon, A. B. Lee, M. Maggioni, B. Nadler, F. Warner, and S. W. Zucker. Geometric diffusions as a tool for harmonic analysis and structure definition of data: Diffusion maps. *PNAS*, 102(21):7426–7431, 2005. 1

[12] E. Corman, M. Ovsjanikov, and A. Chambolle. Continuous matching via vector field flow. *Computer Graphics Forum*, 34(5):129–139, 2015. 1

[13] K. Glashoff and M. M. Bronstein. Optimization on the biorthogonal manifold. *arXiv:1609.04161*, 2016. 4, 7

[14] Q. Huang, F. Wang, and L. Guibas. Functional map networks for analyzing and exploring large shape collections. *ACM Trans. Graphics*, 33(4):36:1–36:11, July 2014. 2, 4, 5, 6

[15] V. Kim, Y. Lipman, and T. Funkhouser. Blended intrinsic maps. *ACM Trans. Graphics*, 30(4), 2011. 5

[16] V. G. Kim, Y. Lipman, and T. Funkhouser. Blended intrinsic maps. *TOG*, 30(4):79, 2011. 1

[17] A. Kovnatsky, M. M. Bronstein, X. Bresson, and P. Vandergheynst. Functional correspondence by matrix completion. In *Proc. CVPR*, 2015. 2, 5

[18] A. Kovnatsky, M. M. Bronstein, A. M. Bronstein, K. Glashoff, and R. Kimmel. Coupled quasi-harmonic bases. *Computer Graphics Forum*, 32:439–448, 2013. 2, 3

[19] B. Lévy. Laplace-Beltrami eigenfunctions towards an algorithm that understands geometry. In *Proc. SMI*, 2006. 5

[20] O. Litany, E. Rodolà, A. M. Bronstein, M. M. Bronstein, and D. Cremers. Non-rigid puzzles. *Computer Graphics Forum*, 35(5), 2016. 7

[21] R. Litman, A. M. Bronstein, and M. M. Bronstein. Diffusion-geometric maximally stable component detection in deformable shapes. *Computers & Graphics*, 35(3):549–560, 2011. 1

[22] J. Masci, D. Boscaini, M. Bronstein, and P. Vandergheynst. Geodesic convolutional neural networks on Riemannian manifolds. In *Proc. 3dRR*, 2015. 1

[23] F. Mémoli. Gromov-Wasserstein distances and the metric approach to object matching. *Foundations of Computational Mathematics*, pages 1–71, 2011. 1

[24] F. Mémoli and G. Sapiro. A theoretical and computational framework for isometry invariant recognition of point cloud

data. *Foundations of Computational Mathematics*, 5(3):313–347, 2005. 1

[25] M. Meyer, M. Desbrun, P. Schröder, and A. H. Barr. Discrete differential-geometry operators for triangulated 2-manifolds. *Visualization and Mathematics III*, pages 35–57, 2003. 5

[26] M. Ovsjanikov, M. Ben-Chen, J. Solomon, A. Butscher, and L. Guibas. Functional maps: A flexible representation of maps between shapes. *ACM Trans. Graphics*, 31(4), 2012. 1, 2, 3, 4, 5, 6

[27] M. Ovsjanikov, Q. Mérigot, F. Mémoli, and L. Guibas. One point isometric matching with the heat kernel. *Computer Graphics Forum*, 29(5):1555–1564, 2010. 1

[28] U. Pinkall and K. Polthier. Computing discrete minimal surfaces and their conjugates. *Experimental Mathematics*, 2:15–36, 1993. 5

[29] J. Pokrass, A. M. Bronstein, M. M. Bronstein, P. Sprechmann, and G. Sapiro. Sparse modeling of intrinsic correspondences. *Computer Graphics Forum*, 32:459–468, 2013. 2, 4

[30] E. Rodolà, A. M. Bronstein, A. Albarelli, F. Bergamasco, and A. Torsello. A game-theoretic approach to deformable shape matching. In *Proc. CVPR*, 2012. 1

[31] E. Rodolà, L. Cosmo, M. M. Bronstein, A. Torsello, and D. Cremers. Partial functional correspondence. *Computer Graphics Forum*, 2016. 2, 4, 5, 7

[32] E. Rodolà, M. Moeller, and D. Cremers. Point-wise map recovery and refinement from functional correspondence. In *Proc. VMV*, 2015. 3

[33] E. Rodolà, S. Rota Bulò, T. Windheuser, M. Vestner, and D. Cremers. Dense non-rigid shape correspondence using random forests. In *Proc. CVPR*, 2014. 1

[34] J. Solomon, A. Nguyen, A. Butscher, M. Ben-Chen, and L. Guibas. Soft maps between surfaces. *Computer Graphics Forum*, 31:1617–1626, 2012. 1

[35] F. Tombari, S. Salti, and L. Di Stefano. Unique signatures of histograms for local surface description. In *Proc. ECCV*, 2010. 6

[36] O. van Kaick, H. Zhang, G. Hamarneh, and D. Cohen-Or. A survey on shape correspondence. *Computer Graphics Forum*, 20:1–23, 2010. 1

[37] M. Vestner, R. Litman, A. M. Bronstein, E. Rodolà, and D. Cremers. Bayesian inference of bijective non-rigid shape correspondence. *arXiv:1607.03425*, 2016. 1, 3

[38] T. Windheuser, U. Schlickwei, F. R. Schimdt, and D. Cremers. Large-scale integer linear programming for orientation preserving 3d shape matching. *Computer Graphics Forum*, 30(5):1471–1480, 2011. 1

[39] T. Windheuser, M. Vestner, E. Rodolà, R. Triebel, and D. Cremers. Optimal intrinsic descriptors for non-rigid shape analysis. In *Proc. BMVC*. BMVA Press, 2014. 1

[40] A. Zaharescu, E. Boyer, K. Varanasi, and R. Horaud. Surface feature detection and description with applications to mesh matching. In *Proc. CVPR*, 2009. 1

[41] Y. Zeng, C. Wang, Y. Wang, X. Gu, D. Samaras, and N. Paragios. Dense non-rigid surface registration using high-order graph matching. In *Proc. CVPR*, 2010. 1